Processing and Application of Ceramics 18 [4] (2024) 366–374
https://doi.org/10.2298/PAC2404366A

Room temperature ethanol sensors using V_2O_5 nanoparticles annealed at different temperatures

Vahid Amiri[1], Ali Mirzaei[1,*], Hossein Roshan[2], Mohammad Hossein Sheikhi[3]

[1]*Department of Materials Science and Engineering, Shiraz University of Technology, Shiraz 71555-13876, Iran*
[2]*Photonic Nanomaterials, Istituto Italiano di Tecnologia, Via Morego 30, Genova 16163, Italy*
[3]*School of Electrical and Computer Engineering, Shiraz University, Shiraz 51154-71348, Iran*

Received 5 August 2024; Received in revised form 3 November 2024; Accepted 13 November 2024

Abstract

In this work V_2O_5 nanoparticles (NPs) were synthesized via a facile Pechini sol-gel route from NH_4VO_3. The as-synthesized amorphous NPs were annealed at three different temperatures, i.e. 350, 450 and 550 °C for 2 h, to study the effect of annealing temperature on the gas sensing performance of the crystalline V_2O_5 NPs. Different characterizations were performed on the synthesized materials to explore their chemical, morphological and structural features. Ethanol gas sensing properties of the annealed V_2O_5 NPs were explored at room temperature with a response of 20 to 1600 ppm ethanol gas. The sensor annealed at 450 °C, indicated the highest sensing response of ~37% to 1600 ppm ethanol vapour along with good selectivity and repeatability. The boosted sensing properties of the optimized gas sensor were related to the optimization of crystallinity and particle size after annealing at 450 °C. Thus, proper choice of annealing temperature is important to realize the sensors with high sensing performance.

Keywords: *V_2O_5 nanopowders, Pechini sol-gel route, structural characterization, ethanol sensors*

I. Introduction

Ethanol (C_2H_5OH), as an important member of volatile organic compound (VOC) family, is widely used as solvent in chemical and food industries [1]. Furthermore, it is widely used as a beverage and unfortunately alcohol drinking is one of the major causes of car accidents globally. The exposure to ethanol causes headache and drowsiness at low concentrations and liver damage and breathing problems at high concentrations [2]. In addition, ethanol is explosive in the range of 3.3 to 19 vol.% in air [3]. Interestingly, ethanol is also a biomarker for obesity-related liver disease [4]. Therefore, the detection of ethanol is vital from different points of view.

Currently, gas sensors are widely used in a couple of applications for public safety, environmental monitoring of hazardous gases, exhaled breath monitoring, etc. [5]. Among available gas sensors, semiconducting metal oxides have unique features including high sensitivity and stability, low price, fast dynamics, simple fabrication and small size [6]. They can be used for the detection of various VOCs such as ethanol [7], acetone [8] and so on. Their working principle is based on the resistance modulation when exposed to gases and thus, by simply measuring the resistance, it is possible to evaluate the sensing response to targeted gases [9,10]. However, one of their main disadvantages is high sensing temperature, which limits their application in remote areas due to high power consumption and the need for frequent battery changes.

Among different vanadium oxides, such as VO, VO_2, V_2O_3, V_3O_7, V_4O_9, V_6O_{13} and V_2O_5, the latter oxide has been widely investigated in the field of gas sensors thanks to its high stability and unique electrical properties [11]. Vanadium pentoxide (V_2O_5) as a semiconducting metal oxide with narrow band gap of 2.3 eV has unique electrical and optical properties [12]. Furthermore, V_2O_5 is relatively abundant, has catalytic activity and can be easily synthesized by various methods [13]. Thanks to these features, it has been used for realization

* Corresponding author: +98737211984
e-mail: *mirzaei@sutech.ac.ir*

of gas sensors [14], batteries [15], detectors [16], supercapacitors [17], energy storage devices and catalysts [18]. In spite of its high potential in gas sensing field, in comparison with SnO_2 and ZnO, it has captured less attention [19]. It should be noted that due to high conductivity of V_2O_5 at room temperature (RT), gas sensors fabricated from V_2O_5 can be used at this low temperature [20–22], which remarkably reduces the power consumption of gas sensors, facilitating the application in remote areas with shortage of power.

For gas sensing studies, different parameters such as particle size, chemical composition and crystalline nature of sensing layer greatly affect the gas sensing performance [23–25]. Upon decrease of particle size, the surface area increases, resulting in availability of more adsorption sites for the targeted gases and a higher sensitivity is expected. Also, when the crystallinity is high, a better conduction through the crystal lead to an enhanced gas response. Generally, increase of crystallinity is performed through annealing at higher temperatures, which results in the growth of particle sizes. Therefore, it is necessary to find optimal annealing temperature to obtain the best sensing performance. Surprisingly, the systematic study of particle size and crystallinity of pristine V_2O_5 nanoparticles (NPs) for gas sensing studies has not been reported yet.

Herein, we synthesized V_2O_5 NPs by a simple Pechini sol-gel route. Subsequently, the synthesized products were annealed at three temperatures, namely 350, 450 and 550 °C for 2 h. The gas sensors were fabricated and the effect of annealing temperature on their gas sensing performance was evaluated at RT. It was revealed that the V_2O_5 NPs annealed at 450 °C had the highest sensing performance to ethanol. A balance between crystallinity and particle size resulted in the highest response to ethanol gas. The results of this study highlight the significant effect of annealing temperature on the gas sensing response of V_2O_5 gas sensors, which should be optimized.

II. Experimental

2.1. Synthesis of V_2O_5 NPs

Ammonium metavanadate (NH_4VO_3), ethylene glycol (EG; $C_2H_6O_2$) and citric acid monohydrate ($C_6H_8O_7 \cdot H_2O$) were employed as starting materials. Initially, NH_4VO_3 was dissolved in distilled water at 70 °C for 1 h to obtain solution with concentration of 0.2 M and in a separate beaker citric acid solution (concentration of 0.4 M) was obtained by dissolving $C_6H_8O_7 \cdot H_2O$ in distilled water also at 70 °C for 1 h. Subsequently, the citric acid solution was slowly added to the NH_4VO_3 solution and later on the esterification agent (EG) was added too. The prepared solution was dried at 120 °C for 12 h to yield the rigid skeleton of powder. Finally, the samples were annealed at different temperatures (350, 450 and 550 °C) for 2 h. The resultant powders were ground in an agate mortar and final V_2O_5 powders were obtained. Figure 1 schematically exhibits the synthesis steps for preparation of V_2O_5 NPs.

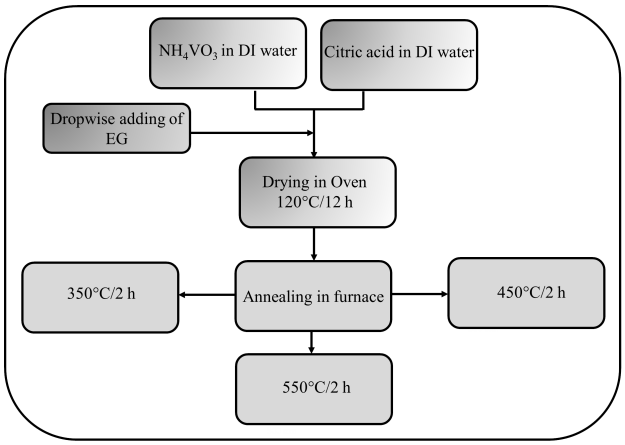

Figure 1. Schematic representation of different steps used for the synthesis of V_2O_5 NPs

2.2. Characterization

The crystallinity of the products was explored by XRD (Philips X'Pert MRD) using CuKα radiation (λ = 1.5418 Å). The morphological features were examined by field-emission scanning electron microscopy (FE-SEM; MIRA3 TESCAN-XMU). Energy dispersive X-ray spectroscopy (EDS) incorporated in FE-SEM was employed for compositional studies. FTIR spectra (Golden Gate Diamond ATR accessory; Bruker Tensor II) were recorded in a wavelength range from 400 to 4000 cm^{-1}. The characteristic bonds vibrations in the samples were examined by Raman spectra (Lab Ram HR; Horiba) with a 532 nm laser. UV-Vis spectra were acquired using a UV-visible spectrophotometer (Shimadzu, UV-1280, Japan) and nitrogen adsorption-desorption isotherms were acquired by BELSORP MINI II at 77 K.

2.3. Gas sensing tests

Alumina substrates with interdigitated Pd-Ag electrodes were used as sensor substrates. The V_2O_5 NPs were mixed with water and then they were precisely drop-coated onto the substrate to form a uniform layer. After evaporation of water, the fabricated gas sensors were connected to a digital multimeter (HIOKI, 3801-50) and put into a gas chamber having volume of 10 l. Then, desired amount of the targeted gas was injected into the chamber using a mass flow controller (MFC). For VOC gases such as ethanol and toluene, desired amounts were calculated and then injected into gas chamber using a syringe. Resistance values of gas sensors were continuously recorded in both air (R_a) and target gas (R_g) atmospheres and the response (%) was defined as:

$$R(\%) = \frac{R_g + R_a}{R_a} \times 100 \quad (1)$$

III. Results and discussion

3.1. Structural, morphological and chemical studies

Figure 2 shows XRD patterns of the V_2O_5 NPs annealed at various temperatures. After annealing the formation of crystalline phase was observed and XRD peaks related to crystalline orthorhombic V_2O_5, matching with JCPD File No. 041-1426, were detected [26]. The intensity of the XRD peaks for the V_2O_5 powder annealed at 350 °C was weaker than those of other two samples, demonstrating weaker crystalline nature of this sample, as expected. Upon increase of crystallization temperature, the intensity of peaks gradually increased, confirming higher crystallinity of the samples at higher temperatures. It should be noted that in the XRD pattern of the sample annealed at 450 °C, some minor peaks other than V_2O_5 phase have appeared, which could be related to the presence of V_3O_7 [27]. These peaks were not observed in the XRD pattern of the sample annealed at 350 °C, possibly due to very low amount of this phase and low crystallinity at this temperature. In addition, at 550 °C the XRD peaks of the formed minor phase disappeared due to its complete conversion to V_2O_5 phase. However, in the sample annealed at 450 °C, overall, amount of the minor phase is extremely low in comparison with V_2O_5 and hence it has no significant effect on the sensing performance.

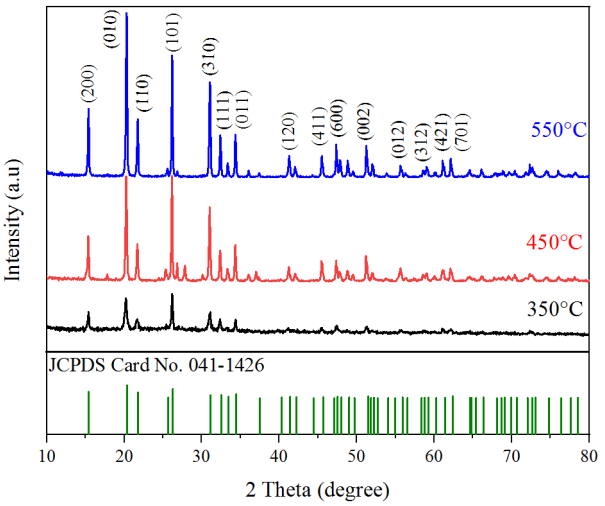

Figure 2. XRD patterns of V_2O_5 NPs annealed at: a) 350 °C, b) 450 °C and c) 550 °C

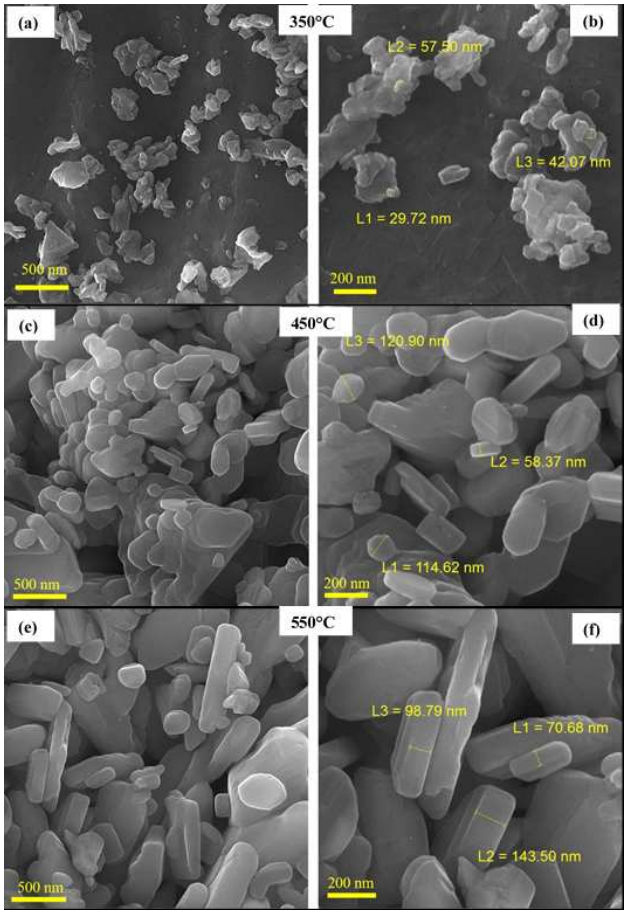

Figure 3. FE-SEM images of V_2O_5 NPs annealed at: (a,b) 350 °C, (c,d) 450 °C and (e,f) 550 °C

Crystallite sizes of the annealed samples were calculated from the most intense peak using Scherrer equation [28]:

$$D = \frac{0.89 \cdot \lambda}{\beta \cdot \cos\theta} \tag{2}$$

where λ is the CuK_α wavelength, β is the full width at half maximum of the most intense peak and θ is Bragg angle. Calculated crystallite sizes of the samples annealed at 350, 450 and 550 °C, were ~35, ~45 and ~56 nm, respectively, i.e. by increasing the annealing temperature, the crystalline size increased. Thus, the sample annealed at higher temperature showed both higher crystallinity and larger crystallite size.

FE-SEM images of the V_2O_5 NPs annealed at different temperatures, i.e. at 350, 450 and 550 °C, are

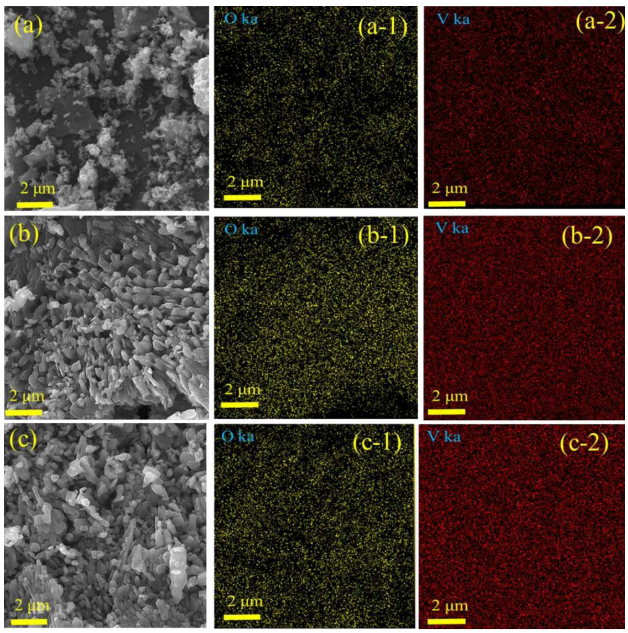

Figure 4. EDS elemental mapping analyses of V_2O_5 NPs annealed at: a) 350 °C, b) 450 °C and c) 550 °C

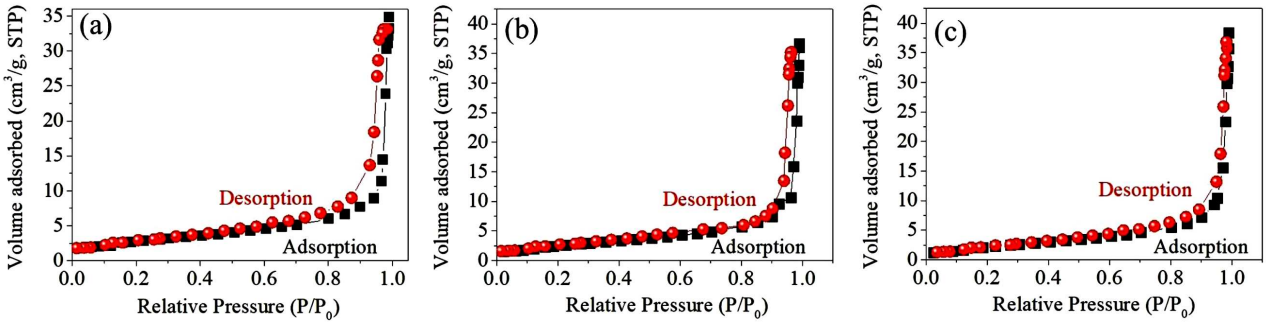

Figure 5. N_2 adsorption-desorption isotherms of V_2O_5 particles annealed at: a) 350 °C, b) 450 °C and c) 550 °C

shown in Fig. 3. Even though the samples show almost the same morphology, it seems that with increasing of the annealing temperature, the size of particles has been slightly increased, in agreement with crystallite sizes calculated from XRD patterns. Figure 4 shows EDS elemental mapping analysis of the V_2O_5 NPs annealed at different temperatures. There is no segregation or discontinuity in chemical composition and in all cases, both O and V elements have been evenly distributed over the entire surface of synthesized materials.

To further illustrate the role of annealing temperature on structure of the prepared powders, nitrogen adsorption-desorption isotherms of different sensors were acquired (Fig. 5). The specific surface areas, calculated using BET approach, were 7.3, 7.2 and 6.2 m^2/g for the V_2O_5 powders annealed at 350, 450 and 550 °C, respectively. The decreased specific surface area upon annealing is in agreement with XRD and FE-SEM results.

Figure 6 indicates FTIR spectra of all samples annealed at different temperatures. The characteristic peaks of the V_2O_5 sample annealed at 550 °C are located at 402, 799 and 1005 cm^{-1} related to the V_3–O, V–O–V vibrations and V=O stretching, respectively, without any sign of impurities [29]. FTIR spectrum of the sample annealed at 450 °C has the same peaks with a slight shift, while for the sample annealed at lower temperature, two additional small peaks related to residual organic species were detected.

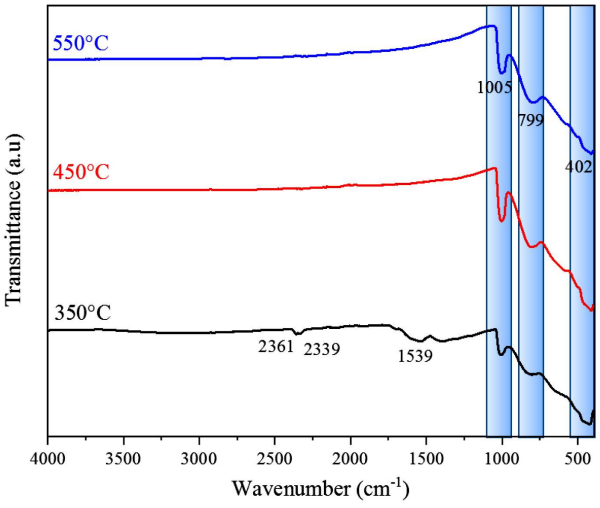

Figure 6. FTIR spectra of V_2O_5 NPs annealed at various temperatures

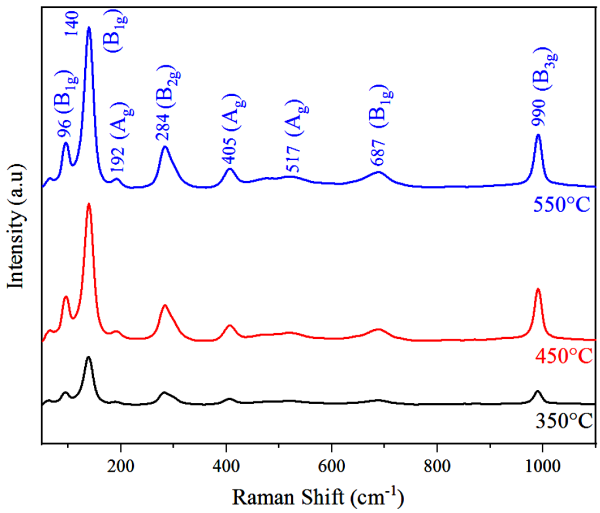

Figure 7. Raman spectra of V_2O_5 NPs annealed at various temperatures

Figure 7 exhibits the Raman spectra of the V_2O_5 NPs annealed at different temperatures. All samples exhibited the characteristic modes of vanadium oxide (V_2O_5). The peaks at 92 and 191 cm^{-1} were ascribed to vibrational modes of layered structure of V_2O_5. The peak at 131 cm^{-1} was due to V=O vibrational mode and the peaks at 274 and 406 cm^{-1} were related to the folding of V=O. The peak at 522 cm^{-1} was attributed to the V–O–V bond stretching and the peak at 688 cm^{-1} was assigned to the V–O stretching vibrational mode. The band at 990 cm^{-1} is generated by the stretching of V=O, demonstrating the existence of layer-type structure of V_2O_5 [30,31].

Optical properties of the synthesized V_2O_5 NPs were also investigated and corresponding UV-Vis spectra of the powders annealed at various temperatures are shown in Fig. 8. The UV-Vis spectra are very similar and were used to calculate band gap energies of all samples by using the Tauc plots, shown in Figs. 8b-d. The calculated band gaps of the samples crystallized at 350, 450 and 550 °C were 2.27, 2.24 and 2.25 eV, respectively, which is close to the reported values in literature [32].

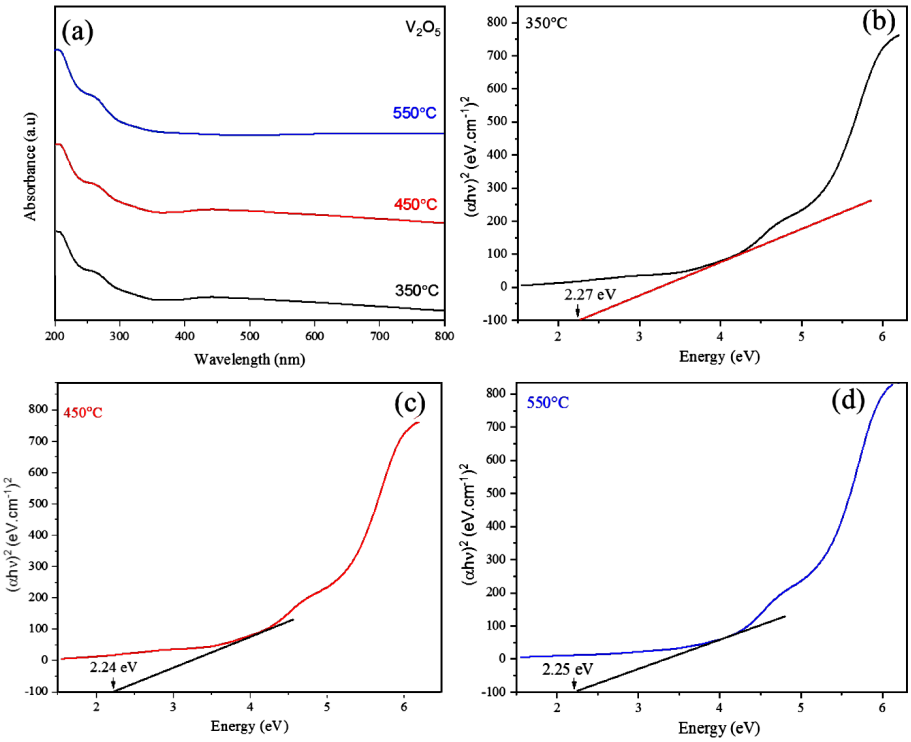

Figure 8. UV-Vis absorption spectra of V_2O_5 NPs annealed at different temperatures (a) and Tauc plots of V_2O_5 NPs annealed at: b) 350 °C, c) 450 °C and d) 550 °C

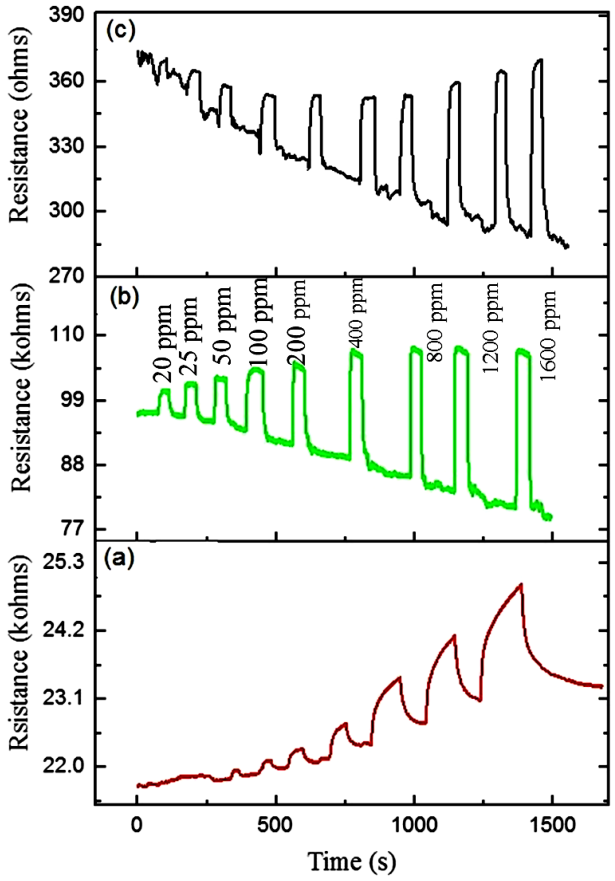

Figure 9. Dynamic resistance curves of V_2O_5 NPs annealed at: a) 350 °C, b) 450 °C and c) 550 °C to various amounts of ethanol at 21 °C

3.2. *Gas sensing studies*

Figure 9a-c indicates dynamic resistance graphs of the V_2O_5 NPs annealed at 350, 450 and 550 °C to various amounts of ethanol at RT (21 °C) and Fig. 10 gives relevant calibration curves of different gas sensors to ethanol gas at 21 °C. Based on dynamic resistance curves, all sensors showed *p*-type behaviour, in which their resistance increased upon introduction of ethanol vapour into gas chamber. Also, based on calibration curves, the response enhanced with increasing of the ethanol concentration, thanks to more adsorption of ethanol on the sensor surface at higher concentrations.

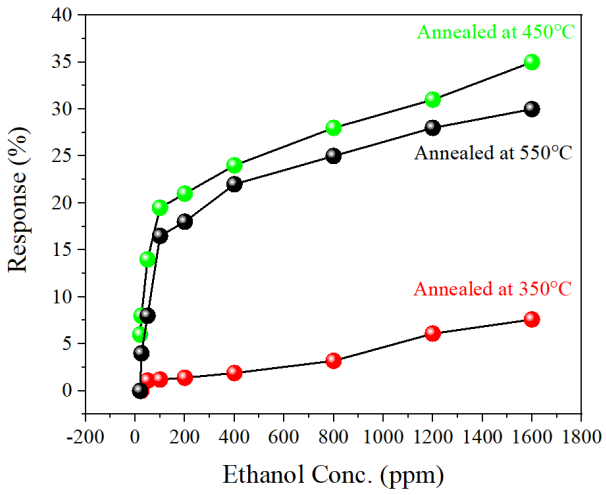

Figure 10. Calibration graphs of V_2O_5 gas sensors towards ethanol at 21 °C

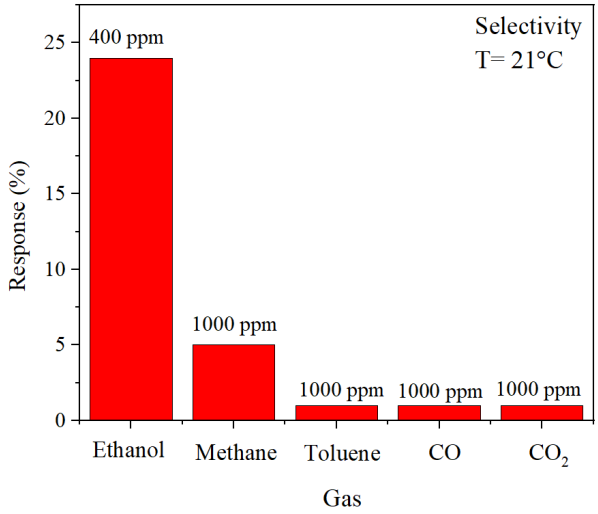

Figure 11. Selectivity histograms of different gas sensors to various gases at 21 °C

Among three different gas sensors, the sensor annealed at 450 °C, revealed the highest response to ethanol gas. Hence, the sensor annealed at 450 °C was exposed to different gases to explore its selectivity behaviour. Figure 11 reveals the selectivity histogram of optimal gas sensor to various gases at 21 °C. Obviously, the sensor indicated a higher response to 50 ppm ethanol gas relative to 10000 ppm methane, 100 ppm CO and 1000 ppm CO_2 and toluene gases. Even though both gas sensors calcined at 350 and 550 °C show almost no response to CO, CO_2 and toluene gases, their response to ethanol is lower than for the sensor calcined at 450 °C.

Figure 12a exhibits repeatability test to 400 ppm ethanol over five sequential cycles for the optimized gas sensor and Fig. 12b offers response versus number of cycles. There are no noticeable differences between the responses during different sensing cycles, demonstrating good repeatability of optimal gas sensor. Finally, we studied the long-term stability of optimal gas sensor by exposing to 400 ppm ethanol after 6, 12 and 18 months. The sensor showed negligible variations in the response even after 18 months, demonstrating its good long-term stability (Fig. 13).

3.3. Proposed sensing mechanism

Resistance gas sensor can sense the presence of a gas in their surrounding atmosphere by generation of an electrical signal related to change of their electrical resistance [33,34]. In this study, V_2O_5 nanostructure gas sensors revealed *p*-type semiconducting behaviour, which has also been reported previously [35]. Thus, the sensing mechanism can be related to the creation of hole accumulation layer (HAL) on the sensor surface and variation of its thickness upon exposure to gas [36,37]. At first in air, oxygen gas is easily adsorbed on the surface of gas sensors and thanks to its high electrophilic nature, it becomes chemisorbed on the surface of sensors by abstracting of electrons [38–40]:

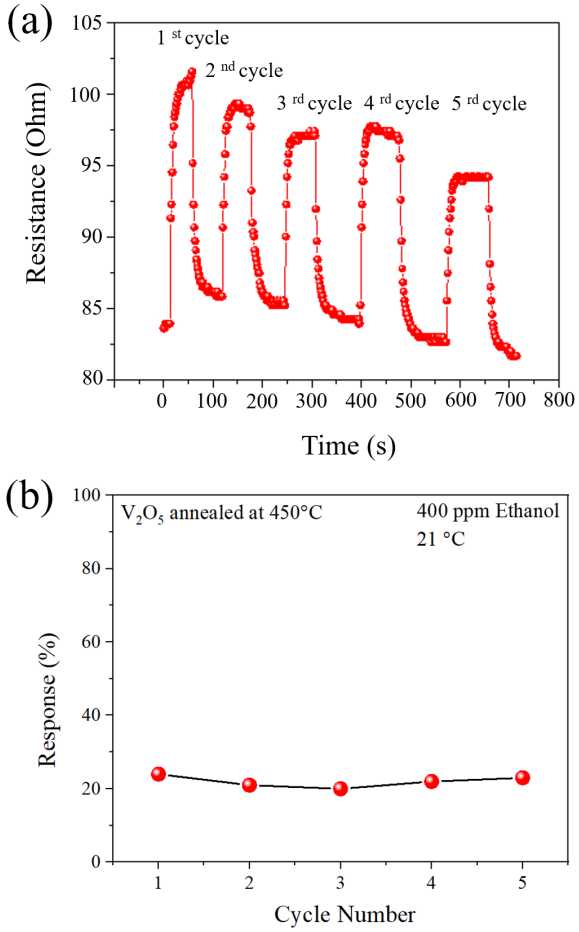

Figure 12. Repeatability test towards 400 ppm ethanol during five sequential cycles at 21 °C (a) and corresponding response versus number of cycles (b)

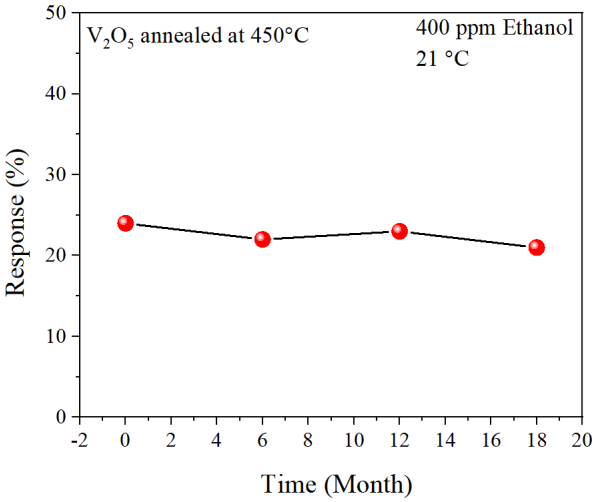

Figure 13. Long-term stability of V_2O_5 gas sensor annealed at 450 °C to 400 ppm ethanol at 21 °C

$$O_2(g) \longrightarrow O_2(ads) \quad (3)$$

$$O_2(ads) + e^- \longrightarrow O_2^- \quad (4)$$

Upon abstraction of electrons, a HAL is formed on the surface of V_2O_5 particle. Due to the presence of this layer, the resistance of *p*-type gas sensors is low in air [41]. By subsequent exposure to ethanol following reaction is expected:

$$C_2H_5OH + 3\,O_2^- \longrightarrow 2\,CO_2 + 3\,H_2O + 3\,e^- \quad (5)$$

Accordingly, due to the release of electrons and subsequent combination with holes in V_2O_5, the width of HAL decreases, causing increase of the sensor resistance. Hence, a sensing signal is generated. Figure 14a schematically presents above mentioned sensing mechanism.

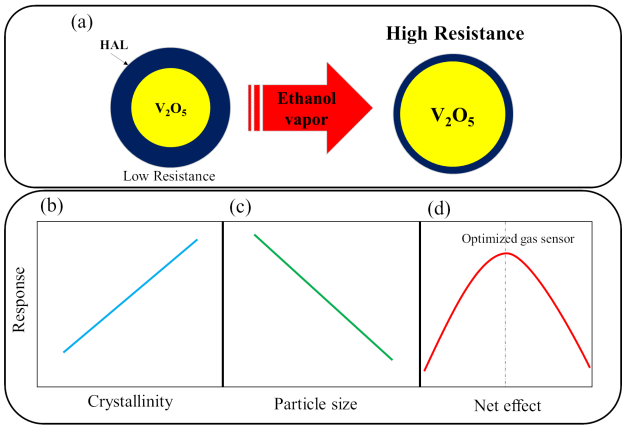

Figure 14. Schematic of ethanol gas sensing mechanism of V_2O_5 gas sensors (a) and effect of crystalline (b), particle size (c) and net effect of crystallinity and particle size (d) on the gas response

Why the sensor annealed at 450 °C indicated the enhanced response to ethanol relative to other gas sensors? It can be related to two factors namely crystallinity and particle size [42]. In fact, higher crystallinity of metal oxides leads to a higher modulation of the resistance in the targeted gas atmosphere [42]. Therefore, considering only crystallinity effect, it can be concluded that the sensor annealed at 550 °C should have a higher response than that annealed at 450 °C due to better crystallinity (Fig. 14b). However, another factor, i.e. particle size also should be considered which shows a reverse trend in comparison with crystallinity (Fig. 14c). The particle size of the sensor annealed at 550 °C is larger than that annealed at 450 °C, thus the sensor can provide lesser number of adsorption sites (smaller surface area) relative to that annealed at 450 °C and considering two mentioned effects, the sensor annealed at 450 °C indicated a higher response to ethanol (Fig. 14d).

It is expected that the sensor will show a higher response to higher concentrations of interfering gases and a similar trend as Fig. 10 is anticipated for it. In fact, when high amounts of interfering gases (more than 1%) is present in surrounding atmosphere of the sensor, a higher response relative to 400 ppm ethanol can be expected. However, in this research the main goal was to investigate the effect of annealing temperature on the sensing performance. Some modifications of the sensors are necessary for practical applications. For example, to have a more selective sensor, the selectivity can be increased by decoration with noble metals such as Au NPs. Also, to further increase the response of the sensor, it can be composited with metal oxides such as SnO_2.

IV. Conclusions

V_2O_5 NPs were prepared via a simple Pechini sol-gel method for ethanol sensing studies. The synthesized products were annealed at different temperatures of 350, 450 and 550 °C for 2 h. Morphology, phase, crystallinity and chemical composition of prepared products were explored through SEM, XRD, Raman and FTIR analyses. It was found that the gas sensor prepared from V_2O_5 NPs annealed at 450 °C exhibited the highest sensing performance to ethanol gas at room temperature. Underlying sensing mechanism was discussed and enhanced sensing capabilities were related to the optimized crystallinity and particle size of the sensor annealed at 450 °C. The results of the present study highlight the remarkable effect of annealing temperature on the gas response which should be optimized to achieve the highest sensing performance.

Acknowledgements: We thank Shiraz University of Technology.

References

1. K. Shingange, H.C. Swart, G.H. Mhlongo, “Design of porous p-type $LaCoO_3$ nanofibers with remarkable response and selectivity to ethanol at low operating temperature”, *Sensors Actuat. B Chem.*, **308** (2020) 127670.
2. S. Choi, M. Bonyani, G.-J. Sun, J.K. Lee, S.K. Hyun, C.J.A.S.S. Lee, “Cr_2O_3 nanoparticle-functionalized WO_3 nanorods for ethanol gas sensors”, *Appl. Surf. Sci.*, **432** [Part B] (2018) 241–249.
3. H.R. Yousefi, B. Hashemi, A. Mirzaei, H. Roshan, M.H. Sheikhi, “Effect of Ag on the ZnO nanoparticles properties as an ethanol vapor sensor”, *Mater. Sci. Semiconduc. Process.*, **117** (2020) 105172.
4. S. Nair, K. Cope, R.H. Terence, A.M. Diehl, “Obesity and female gender increase breath ethanol concentration: potential implications for the pathogenesis of nonalcoholic steatohepatitis”, *Am. J. Gastroenter.*, **96** [4] (2001) 1200–1204.
5. K. Wetchakun, T. Samerjai, N. Tamaekong, C. Liewhiran, C. Siriwong, V. Kruefu, A. Wisitsoraat, A. Tuantranont, S.J.S. Phanichphant, A.B. Chemical, “Semiconducting metal oxides as sensors for environmentally hazardous gases”, *Sensors Actuat. B Chem.*, **160** [1] (2011) 580–591.
6. A. Mirzaei, S.G. Leonardi, G. Neri, “Detection of hazardous volatile organic compounds (VOCs) by metal oxide nanostructures-based gas sensors: A review”, *Ceram. Int.*, **42** [14] (2016) 15119–15141.
7. S.G. Leonardi, A. Mirzaei, A. Bonavita, S. Santangelo, P. Frontera, F. Pantò, P.L. Antonucci, G. Neri, “A comparison of the ethanol sensing properties of α-iron oxide nanostructures prepared via the sol-gel and electrospinning techniques”, *Nanotechnology*, **27** [7] (2016) 075502.

8. B. Boudart, Y. Guhel, N. Lamrani-Amaouz, R. Douani, A. Chaouchi, "Enhanced volatile organic compound sensing properties of $BiFeO_3$ by carbon fibres addition", *Process. Appl. Ceram.*, **16** [4] (2022) 310–320.
9. A. Mirzaei, J.-H. Kim, H.W. Kim, S.S. Kim, "Resistive-based gas sensors for detection of benzene, toluene and xylene (BTX) gases: A review", *J. Mater. Chem. C*, **6** [16] (2018) 4342–4370.
10. A. Mirzaei, S.S. Kim, H.W. Kim, "Resistance-based H_2S gas sensors using metal oxide nanostructures: A review of recent advances", *J. Hazardous Mater.*, **357** (2018) 314–331.
11. R. Alrammouz, M. Lazerges, J. Pironon, I.B. Taher, A. Randi, Y. Halfaya, S. Gautier, "V_2O_5 gas sensors: A review", *Sensors Actuat. A Phys.*, **332** (2021) 113179.
12. N. Singh, A. Umar, N. Singh, H. Fouad, O.Y. Alothman, F.Z. Haque, "Highly sensitive optical ammonia gas sensor based on Sn doped V_2O_5 nanoparticles", *Mater. Res. Bull.*, **108** (2018) 266–274.
13. V. Amiri, H. Roshan, A. Mirzaei, M.H. Sheikhi, "A review of nanostructured resistive-based vanadium oxide gas sensors", *Chemosensors*, **8** [4] (2020) 105.
14. W. Yan, M. Hu, D. Wang, C. Li, "Room temperature gas sensing properties of porous silicon/V_2O_5 nanorods composite", *Appl. Surf. Sci.*, **346** (2015) 216–222.
15. Y. Liu, M. Clark, Q. Zhang, D. Yu, D. Liu, J. Liu, G.J.A.E.M. Cao, "V_2O_5 nano-electrodes with high power and energy densities for thin film Li-ion batteries", *Adv. Energy Mater.*, **1** [2] (2011) 194–202.
16. P.D. Raj, S. Gupta, M. Sridharan, "Studies on nanostructured V_2O_5/V/V_2O_5 films for un-cooled IR detector application", *J. Mater. Sci. Mater. Electron.*, **27** [7] (2016) 7494–7500.
17. Z. Yin, J. Xu, Y. Ge, Q. Jiang, Y. Zhang, Y. Yang, Y. Sun, S. Hou, Y. Shang, Y. Zhang, "Synthesis of V_2O_5 microspheres by spray pyrolysis as cathode material for supercapacitors", *Mater. Res. Express*, **5** [3] (2018) 036306.
18. Y. He, M.E. Ford, M. Zhu, Q. Liu, U. Tumuluri, Z. Wu, I.E.J.A.C.B.E. Wachs, "Influence of catalyst synthesis method on selective catalytic reduction (SCR) of NO by NH_3 with V_2O_5-WO_3/TiO_2 catalysts", *Appl. Catal. B Environmen.*, **193** (2016) 141–150.
19. H.-J. Kim, J.-H.J.S. Lee, A.B. Chemical, "Highly sensitive and selective gas sensors using p-type oxide semiconductors: Overview", *Sensors Actuat. B Chem.*, **192** (2014) 607–627.
20. X. Qiang, M. Hu, L. Zhou, J. Liang, "Pd nanoparticles incorporated porous silicon/V_2O_5 nanopillars and their enhanced p-type NO_2-sensing properties at room temperature", *Mater. Lett.*, **231** (2018) 194–197.
21. P.S. Chauhan, S. Bhattacharya, "Highly sensitive $V_2O_5{\cdot}1.6H_2O$ nanostructures for sensing of helium gas at room temperature", *Mater. Lett.*, **217** (2018) 83–87.
22. M. Amarnath, A. Heiner, K. Gurunathan, "Surface bound nanostructures of ternary r-GO/Mn_3O_4/V_2O_5 system for room temperature selectivity of hydrogen gas", *Ceram. Int.*, **46** [6] (2020) 7336–7345.
23. J.M. Walker, S.A. Akbar, P.A. Morris, "Synergistic effects in gas sensing semiconducting oxide nano-heterostructures: A review", *Sensors Actuat. B Chem.*, **286** (2019) 624–640.
24. P. Karnati, S. Akbar, P.A. Morris, "Conduction mechanisms in one dimensional core-shell nanostructures for gas sensing: A review", *Sensors Actuat. B Chem.*, **295** (2019) 127–143.
25. M. Al-Hashem, S. Akbar, P. Morris, "Role of oxygen vacancies in nanostructured metal-oxide gas sensors: A review", *Sensors Actuat. B Chem.*, **301** (2019) 126845.
26. P. Jing, W. Wei, W. Luo, X. Li, F. Xu, H. Li, M. Wei, D. Yu, Q. Zhu, G. Liu, "In-situ XRD study of the structure and electrochemical performance of V_2O_5 nanosheets in aqueous zinc ion batteries", *Inorg. Chem. Commun.*, **117** (2020) 107953.
27. M.K. Chine, F. Sediri, N., Gharbi, "Hydrothermal synthesis of $V_3O_7{\cdot}H_2O$ nanobelts and study of their electrochemical properties", *Mater. Sci. Appl.*, **2** [8] (2011) 964–970.
28. P. Van Tong, L. Hoang Minh, N. Van Duy, C. Manh Hung, "Porous In_2O_3 nanorods fabricated by hydrothermal method for an effective CO gas sensor", *Mater. Res. Bull.*, **137** (2021) 111179.
29. L.T.B. Mendonça, A.G. Bezerra Jr, W.M. de Azevedo, "Preparation and characterization of V_2O_5 and V_2O_5/PANI nanocomposite by laser ablation technique in liquid", *Mater. Chem. Phys.*, **273** (2021) 125084.
30. R. Suresh, K. Giribabu, R. Manigandan, S. Munusamy, S.P. Kumar, S. Muthamizh, A. Stephen, V. Narayanan, "Doping of Co into V_2O_5 nanoparticles enhances photodegradation of methylene blue", *J. Alloys Compd.*, **598** (2014) 151–160.
31. W.G. Menezes, D.M. Reis, T.M. Benedetti, M.M. Oliveira, J.F. Soares, R.M. Torresi, A.J. Zarbin, "V_2O_5 nanoparticles obtained from a synthetic bariandite-like vanadium oxide: Synthesis, characterization and electrochemical behavior in an ionic liquid", *J. Colloid Interf. Sci.*, **337** [2] (2009) 586–593.
32. C.V. Reddy, I.N. Reddy, R. Koutavarapu, K.R. Reddy, T.A. Saleh, T.M. Aminabhavi, J. Shim, "Novel edge-capped ZrO_2 nanoparticles onto V_2O_5 nanowires for efficient photosensitized reduction of chromium (Cr(VI)), photoelectrochemical solar water-splitting, and electrochemical energy storage applications", *Chem. Eng. J.*, **430** (2022) 132988.
33. A. Dey, "Semiconductor metal oxide gas sensors: A review", *Mater. Sci. Eng. B*, **229** (2018) 206–217.
34. D. Zappa, V. Galstyan, N. Kaur, H.M.M. Arachchige, O. Sisman, E. Comini, "Metal oxide-based heterostructures for gas sensors – A review", *Anal. Chim. Acta*, **1039** (2018) 1–23.
35. P.S. Chauhan, A. Mishra, G. Bhatt, S. Bhattacharya, "Enhanced He gas detection by V_2O_5-noble metal (Au, Ag, and Pd) nanocomposite with temperature dependent n-to p-type transition", *Mater. Sci. Semicond. Process.*, **123** (2021) 105528.
36. T.P. Mokoena, H.C. Swart, D.E. Motaung, "A review on recent progress of p-type nickel oxide based gas sensors: Future perspectives", *J. Alloys Compd.*, **805** (2019) 267–294.
37. P. Salimi Kuchi, H. Roshan, M.H. Sheikhi, "A novel room temperature ethanol sensor based on PbS:SnS_2 nanocomposite with enhanced ethanol sensing properties", *J. Alloys Compd.*, **816** (2020) 152666.
38. N.M. Abd-Alghafour, G.A. Naeem, A.S. Ibraheam, N. Afzal, S.M. Mohammad, R.F. Muslim, "Fabrication and characterization of ethanol gas sensor based on hydrothermally grown V_2O_5 nanorods", *Optik*, **222** (2020) 165441.

39. X. Yang, H. Li, T. Li, Z. Li, W. Wu, C. Zhou, P. Sun, F. Liu, X. Yan, Y. Gao, X. Liang, G. Lu, "Highly efficient ethanol gas sensor based on hierarchical SnO_2/Zn_2SnO_4 porous spheres", *Sensors Actuat. B Chem.*, **282** (2019) 339–346.
40. T.P. Mokoena, K.T. Hillie, H.C. Swart, N. Leshabane, J. Tshilongo, D.E. Motaung, "Fabrication of a propanol gas sensor using p-type nickel oxide nanostructures: The effect of ramping rate towards luminescence and gas sensing characteristics", *Mater. Chem. Phys*., **253** (2020) 123316.
41. S.M. Majhi, G.K. Naik, H.-J. Lee, H.-G. Song, C.-R. Lee, I.-H. Lee, Y.-T. Yu, "Au@NiO core-shell nanoparticles as a p-type gas sensor: Novel synthesis, characterization, and their gas sensing properties with sensing mechanism", *Sensors Actuat. B Chem.*, **268** (2028) 223–231.
42. **A.** Katoch, G.-J. Sun, S.-W. Choi, J.-H. Byun, S.S. Kim, "Competitive influence of grain size and crystallinity on gas sensing performances of ZnO nanofibers", *Sensors Actuat. B Chem.*, **185** (2013) 411–416.